

RICE UNIVERSITY

Electronic Properties and Applications of 2D Materials

by

Henry (Shan An) Yu

A THESIS SUBMITTED
IN PARTIAL FULFILLMENT OF THE
REQUIREMENTS FOR THE DEGREE

Master of Science

APPROVED, THESIS COMMITTEE:

Boris I. Yakobson, Chair
Professor of Materials Science and
Nanoengineering and Chemistry

Douglas Natelson
Professor of Physics and Astronomy,
Electrical and Computer Engineering and
Materials Science and Nanoengineering

Ming Tang
Assistant Professor of Materials Science
and Nanoengineering

Houston, Texas

July, 2016

RICE UNIVERSITY

Electronic Properties and Applications of 2D
Materials

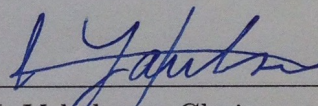
by

Henry (Shan An) Yu

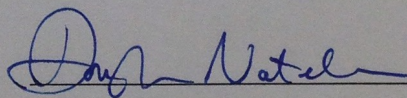
A THESIS SUBMITTED
IN PARTIAL FULFILLMENT OF THE
REQUIREMENTS FOR THE DEGREE

Master of Science

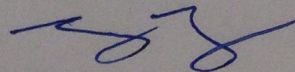
APPROVED, THESIS COMMITTEE:



Boris I. Yakobson, Chair
Professor of Materials Science and
Nanoengineering and Chemistry



Douglas Natelson
Professor of Physics and Astronomy,
Electrical and Computer Engineering and
Materials Science and Nanoengineering



Ming Tang
Assistant Professor of Materials Science
and Nanoengineering

Houston, Texas

July, 2016

RICE UNIVERSITY

Electronic Properties and Applications of 2D
Materials

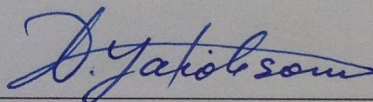
by

Henry (Shan An) Yu

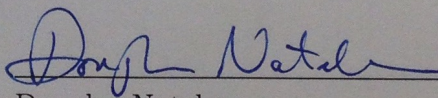
A THESIS SUBMITTED
IN PARTIAL FULFILLMENT OF THE
REQUIREMENTS FOR THE DEGREE

Master of Science

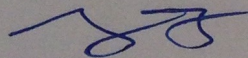
APPROVED, THESIS COMMITTEE:



Boris I. Yakobson, Chair
Professor of Materials Science and
Nanoengineering and Chemistry



Douglas Natelson
Professor of Physics and Astronomy,
Electrical and Computer Engineering and
Materials Science and Nanoengineering



Ming Tang
Assistant Professor of Materials Science
and Nanoengineering

Houston, Texas

July, 2016

ABSTRACT

Electronic Properties and Applications of 2D Materials

by

Henry (Shan An) Yu

2D materials has become one of the most exciting areas of research, since the report of graphene in 2005 [14]. For graphene, the high mobility ($\sim 15,000 \text{ cm}^2\text{V}^{-1}\text{s}^{-1}$) [14] draws much attention to its potential as high speed electronic devices. Its cone-like electronic dispersion, resembling that of relativistic massless Dirac fermions, entertains many exotic and interesting behaviors, making it an ideal system for the study of relativistic particles. Aside from graphene, many other 2D materials have also been successfully made, including MoS_2 , h-BN, 2D Boron, etc. Although these newly made materials have already exhibited several good characteristics, they are also distinctively different from traditional 3D materials. This means that a deeper understanding of 2D materials is imperative, to capture and utilize their unique features. The abundant atomistic modeling methods nowadays enable us to investigate the various aspects of 2D materials (or any system in general), with the help of computers. Density Functional Theory (DFT) based methods can give very accurate descriptions of the ground state properties of materials, including their charge density, mechanical moduli or the optimal structure; on top of DFT, many body theory methods also allow for the construction of excitation processes based on the DFT results. In the case of large structures, in which DFT may not be affordable, the tight-binding method can be an excellent alternative with a much lower cost.

In this work, I will employ these atomistic methods to the understanding of the distinctive features of 2D materials, especially their electronic, or even electro-mechanical properties. First, I have found that the graphite screw dislocations (GSD), a family of graphene-like structures as nanoribbons, turn out to be superior nano-solenoids, producing magnetic field up to 1T at typical voltage. Second, I have successfully modeled the strain-induced Landau quantization of the graphene band structure in large structures ($N \sim 10^5$), showing the possibility of strain engineering for the design of desired Landau levels in actual devices. Finally, I have discovered several universal features for 2D lateral junctions. 2D junctions, due to the weak electronic screening, turn out to be not merely a miniaturized version of its 3D counterpart. The scaling laws, depletion region and several practical consequences are analyzed and quantified.

Contents

Abstract	ii
List of Illustrations	v
1 Introduction	1
2 Graphene Nanosolenoid	3
2.1 Structure of Graphene Solenoid	3
2.2 Simulation of Transport and Magnetism	5
2.3 Performance	7
3 Pseudo-Magnetic Field in Graphene	12
3.1 Strain Induced Gauge Field in Graphene	12
3.2 Pseudo-Landau Levels	14
3.3 Numerical Simulation	15
4 2D Lateral Junction	19
4.1 Thermodynamics of a Heterojunction	19
4.2 3-Dimensional Heterojunction	20
4.3 Theory of 2D Junction	22
4.4 Simulation of Real Material 2D Junction	24
5 Summary	31
Bibliography	32

Illustrations

- 2.1 (a~c) Atomic structure of a graphite screw dislocation, GSD. (a) Axial view with armchair edge, width N_A . (b) Sideview, Burgers vector \mathbf{b} parallel to the dislocation line γ (red). (c) Axial view of ZGSD, width N_Z . (d~f) The calculated band structure of armchair-edge AGSD of widths $N_A = 12, 13, 14$, and of zigzag-edge ZGSD for $N_Z = 7, 8$, and their bandgaps in (e). (Reprinted (adapted) with permission from F. Xu *et al.*, *Nano Letters*, 16,1,34-39, 2016. Copyright 2016 American Chemical Society.) 4
- 2.2 (a,b) Metallic zigzag-edge ZGSD, $N_Z = 9$. (a) Transmission coefficient as a function of energy. (b) Spatial current distribution integrated over various energy ranges of panel (a), left for green region (bias $V = 0.4$ V), middle for green plus blue region ($V = 0.7$ V), right for green plus blue plus yellow region ($V = 2$ V). (c) Bright-dark map of current distribution, for $N_Z = 21$ and bias of 0.4 V. (Reprinted (adapted) with permission from F. Xu *et al.*, *Nano Letters*, 16,1,34-39, 2016. Copyright 2016 American Chemical Society.) 7

2.3	(a)Magnetic field B versus the radial position. The dashed blue lines are obtained by simply scaling the curves of 0.5 V (solid blue) to highlight the deviations from the red curves, actually computed for 1.2 V. For a wider GSD ($N_Z = 21$) the field rise is closer to proportional while change in the pattern lessens. (b)The magnetic flux Φ versus the total current J in a metallic ZGSD of small width $N_Z = 5$ (red) and wider $N_Z = 21$ (green triangles, fitted by the ohmic-solenoid formula, blue line). (Inset) Computed inductance for the atomistic models (circles) and the red curve from the classical model per eq 2.1. (Reprinted (adapted) with permission from F. Xu <i>et al.</i> , <i>Nano Letters</i> , 16,1,34-39, 2016. Copyright 2016 American Chemical Society.)	9
3.1	Shows the schematics of (a)unstrained and (b)strained graphene lattice structure	13
3.2	(a) A 256×256 super cell of graphene flake. (b) DOS of unstrained(green) and strained(blue) graphene.	16
3.3	(a) Atomistic structure of a twisted graphene ribbon. (b) Strain profile in a twisted ribbon.	17
3.4	(a) Band structure and (b) DOS of zig-zag graphene ribbon of width 170 nm. (c) Band structure and (d) DOS of twisted zig-zag graphene ribbon of width 170 nm and twisting rate $0.61^\circ/\text{nm}$. Dashed lines are plotted according to eq 3.4, with $B=60\text{T}$	18
4.1	3D heterojunction of two materials with chemical potentials μ_1^0, μ_2^0 respectively. Charge exchange forms a dipole of width $2w$ at the interface, establishing an electrostatic potential $\phi(x)$ to equilibrate the system.	21

- 4.2 (a) Schematics of a 2D lateral junction, showing how two in-plane charges can have long range interaction via out of plane direction. (b) Schematics of local charge exchange in a 2D junction forming a dipole line, which cannot establish a global potential step. (c) Shows that a delocalized charge exchange is required for the equilibration of the intrinsic chemical potentials. 22
- 4.3 Schematics of a lateral coplanar 2D heterojunction (a) and (b)-(d) of band alignments in the contacts of two metals (b), and semiconductor (c) or graphene (d) p-n junctions. E_F is the equilibrated Fermi level and $\phi(x)$ is the built-in potential within the plane of the materials. Full band structures of a 2D semiconductor (MoS_2) and graphene, with doping levels of -0.1 (red dashed), 0.0 (black solid) and +0.1 (blue dashed) e/cell are shown on the left. Horizontal lines show positions of the Fermi level for each doping degree. (Reprinted (adapted) with permission from Henry *et al.*, *Nano Letters*, 2016, doi:10.1021/acs.nanolett.6b01822. Copyright 2016 American Chemical Society.) 26

- 4.4 Computed electrostatic potential and surface charge density in 2D lateral MoS₂|MoS₂ and graphene|graphene p-n junctions; only the n-doped side is shown. (a) Surface charge density (top) and electrostatic potential (bottom) for symmetrically doped 2D (solid red lines) and 3D bulk (solid blue lines) MoS₂ p-n junctions with doping $p = 10^{-4}$. The asymptotic behavior of eq 2 is shown with a red dashed line; the depletion width $W=48$ nm is marked. (b) Surface charge density (top) and electrostatic potential (bottom) for symmetrically doped lateral 2D and 3D bulk graphene p-n junctions with $p = 1.5 \cdot 10^{-4}$; width $W = 12$ nm of graphene junction is marked. (Reprinted (adapted) with permission from Henry *et al.*, *Nano Letters*, 2016, doi:10.1021/acs.nanolett.6b01822. Copyright 2016 American Chemical Society.) 27
- 4.5 The depletion width W in MoS₂| MoS₂ and Gr|Gr p-n junctions. Red circles show computed widths W_2 of lateral 2D MoS₂ junctions, and the red solid line is from eq 3; blue dashed line shows the depletion width W_3 of a corresponding 3D semiconductor. Red crosses, and the tracking red line show similar results for graphene. Inset compares the depletion widths of 2D (red lines) and 3D (blue dashed lines) semiconductors as functions of the total built-in potential $\Delta\phi - V$; depletion widths W_2 for 2D (red lines) and the widths W_3 for the 3D analog (blue dashed lines) are shown for $p = 10^{-7}, 10^{-5}$, and 10^{-3} . (Reprinted (adapted) with permission from Henry *et al.*, *Nano Letters*, 2016, doi:10.1021/acs.nanolett.6b01822. Copyright 2016 American Chemical Society.) 29

Chapter 1

Introduction

2-Dimensional materials were previously thought impossible to exist, according to Landau's theory on the thermal vibrations of crystal lattice [7]. However, in 2005, a free-standing, atomically thin film of carbon, graphene, was successfully cleaved (with the mighty scotch tape) from graphite [14] [15], to which the 2010 Nobel Prize in Physics was awarded. In fact, many other free-standing 2D materials such as MoS_2 , NbS_2 , h-BN have also been extracted. Although this apparent dichotomy can be resolved after a closer look at both cases, it manifests the exotic behaviors and interesting physics of 2D materials.

Due to the reduction of dimensionality, compared to 3D systems, the governing equations for 2D systems clearly have different forms and can lead to drastically new behaviors. Electronic screening is much weaker in 2D systems, which can lead to various consequences including higher binding energy for excitons, deeper dopant levels in semiconductors, and higher susceptibility to externally applied field (e.g. FET). On the other hand, the lattice vibrations, or phonons, also exhibit different behaviors which result in van Hove singularities and the instability of 2D crystals. Although these new properties may render some traditional applications unworkable, it also opens many pathways to new device designs.

In this thesis I will look at three examples where the distinctive features of 2D materials lead to new physics compared to its 3D counterparts, and potentially new applications. In chapter 2 a study of the structure of a graphene spiral, or a graphite

screw dislocation (GSD), will be presented. Graphitic structures, being so versatile, can be adapted to many shapes, corresponded with different electronic and also mechanical properties [13] [3]. A graphene spiral, similar to graphene nanoribbons [13], can have its electronic band gap controlled by the size and edge type, forming a family of structures including both insulators and conductors. Surprisingly, for certain types of conducting GSDs, they turn out to be extremely high quality nano-solenoids, producing magnetic field up to ~ 1 Tesla, out-performing many current designs. In chapter 3, I will go on to investigate the very interesting phenomenon of strain-induced magnetic field in graphene systems. Due to the electronic structure and lattice symmetry of graphene, theories have suggested the engineering of the graphene states via applied strain [19]. Interestingly, under small strain, the effect of distortion mimics that of a magnetic field, which leads to the Landau quantization of the electronic states near the Fermi level. According to my studies, a pseudo-magnetic field up to 60 Tesla can be easily obtained in certain graphene structures. Finally, in chapter 4, I present a novel theoretical analysis for 2D lateral junctions. Due to weak electronic screening, 2D junctions have drastically different behaviors compared to traditional 3D junctions. I will show how the traditional knowledge of charge exchange, depletion region and length scale should be modified to accurately capture the features of 2D junctions.

Chapter 2

Graphene Nanosolenoid

In this chapter I will present an analysis of the electronic and transport properties of graphite screw dislocations (GSD), and also its performance as a nano-solenoid. In 2.1 I will discuss the structural dependence of the electronic properties of GSDs. In 2.2 I will show a multi-level numerical scheme for the modeling of the transport and magnetic field of a conducting GSD. Finally in 2.3 I will show the calculated results and the performance of GSD as a nano-solenoid. Most of this chapter is adapted from my previously published work [26].

2.1 Structure of Graphene Solenoid

The electronic properties of graphene spirals, or graphite screw dislocations (GSD) depend strongly on its atomic structure. Here as shown in fig 2.1 we study the electronic bandstructures of a GSD with the exterior shape as hexagon, bounded by all armchair or zig-zag edges, AGSD or ZGSD. A screw dislocation Burgers vector \mathbf{b} , where $|\mathbf{b}| = 3.4\text{\AA}$ the natural interlayer spacing for graphene, is assumed. Following the convention of graphene nano ribbons (GNR), the width of the AGSD is defined by counting the dimer lines (N_A) from the inmost atoms to the outermost edge, and the number of zig-zag chains (N_Z) defines the width of ZGSD. We employ a tight-binding framework with nearest and next nearest neighbor hopping parameters $\gamma_0 = -2.7\text{ eV}$ and $\gamma_1 = -0.069\text{ eV}$, respectively; both varying exponentially with the

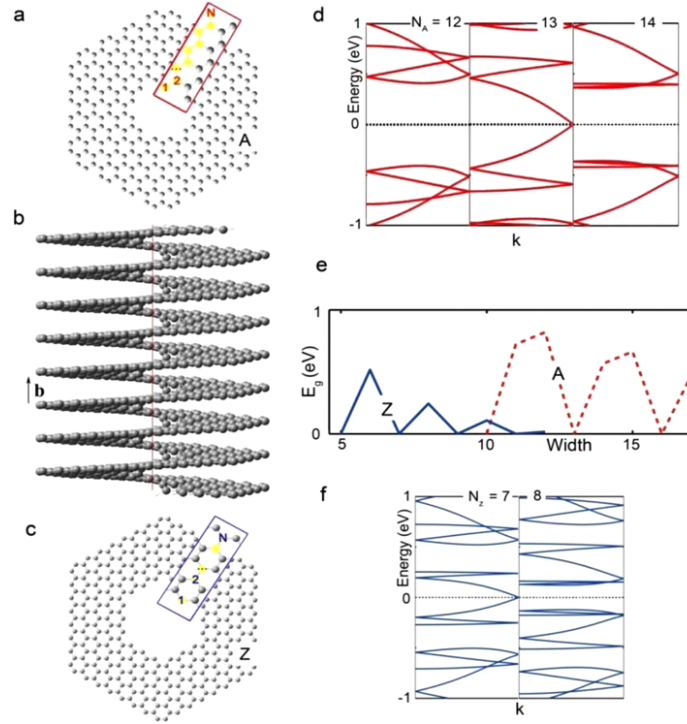


Figure 2.1 : (a~c) Atomic structure of a graphite screw dislocation, GSD. (a) Axial view with armchair edge, width N_A . (b) Sideview, Burgers vector \mathbf{b} parallel to the dislocation line γ (red). (c) Axial view of ZGSD, width N_Z . (d~f) The calculated band structure of armchair-edge AGSD of widths $N_A = 12, 13, 14$, and of zigzag-edge ZGSD for $N_Z = 7, 8$, and their bandgaps in (e). (Reprinted (adapted) with permission from F. Xu *et al.*, *Nano Letters*, 16,1,34-39, 2016. Copyright 2016 American Chemical Society.)

bond length to account for possible deformations [17]. Our calculations show that, in a manner analogous to GNR, the width of the GSD controls whether it is metallic or insulating. As shown in fig 2.1(d)(e), the AGSD will be metallic for $N_A = 3p + 1$ where p is integer, which is very similar to the behavior of AGNR where it is metallic for $N_A = 3p + 2$. As for ZGSDs, as shown in fig 2.1(e)(f), it is metallic for $N_z = 2p + 1$, which is different from the behavior of ZGNR where it is metallic for all widths. In addition, the band gaps of the insulating GSDs, whether A or Z type, decreases to

zero as the width increases, approaching the zero-gap spectrum of graphene. With these analysis, we are able to find the proper metallic GSD according to the width and edge types, and simulate its transport properties, hopefully to find the suitable structure for the use of a nano-solenoid.

2.2 Simulation of Transport and Magnetism

In this section I present the calculation methods employed to asses the GSDs ability as a nanosolenoid. With standard NEGF methods [21] one can easily obtain the current and conductance of a GSD structure, at a given bias voltage. However, to obtain the induced magnetic field and also its inductance, the spatial distribution of the current is required.

Before diving into discussions about the numerical scheme for calculating the current and magnetic field distribution in a GSD structure, it is instructive to first investigate a GSD classically. Here we consider a spiral made of ohmic metallic sheets of conductivity σ , with an inner radius R' and outer radius R , and also a winding density $n = 1/|\mathbf{b}|$. A voltage v per each turn will generate concentric currents $dI = v\sigma bdr/2\pi r$, leading to a total current $I = (v\sigma b/2\pi)\ln(R/R')$. The total magnetic flux normal to the GSD axis is $\Phi = (\mu_0 v\sigma b n/4)(R^2 - R'^2)$, whereas the field profile along the axis is $B(r) = (\mu_0 n v\sigma b/2\pi)\ln(R/r)$. With the formula for the total magnetic energy $\mu_0^{-1} \int B^2(r)\pi r dr = LI^2/2$, one can express the inductance as

$$L = \pi\mu_0 R^2 n^2 g(R'/R) \quad (2.1)$$

where $g(\alpha) = (1/2 + \alpha^2 \ln \alpha - \alpha^2/2)/\ln^2 \alpha$ is a dimensionless factor that accounts for the finite width of the spirals. For an infinitely thin wire $R'/R \rightarrow 1$ we have $g(R'/R) \rightarrow 1$, and eq. 2.1 falls back to the expressoin for the inductance of conducting coils. Eq. 2.1

essentially serves as an asymptotic solution for inductance of graphene GSD with large width.

For a more realistic modeling of the current distribution and magnetic profile of the graphene GSDs, we employ a multi-scale numerical scheme. The magnetic field $B(r)$ can be obtained from the current distribution $i(r)$ via Biot-Savart law. The current distribution can be first broken down into the inter-atomic bond currents $i_{\alpha\beta}$, where α and β represent atomic sites. To calculate $i_{\alpha\beta}$ we start with the energy-resolved inter-atomic site current, which, within the tight-binding framework, can be expressed as [24]

$$di_{\alpha\beta} = \frac{4e}{\hbar} \text{Im}[H_{\alpha\beta} D_{\alpha\beta}(E)] dE \quad (2.2)$$

here $H_{\alpha\beta}$ is the Hamiltonian matrix element, and $D_{\alpha\beta}$ is the density of states, which can be evaluated via real space NEGF methods [24, 27]. The total current flowing through α to β site is therefore $i_{\alpha\beta} = \int di_{\alpha\beta}$. Although $i_{\alpha\beta}$ gives the current among different bonds, it does not give the total spatial distribution of the current. We therefore resort to higher levels of theory, in which the current around a bond can be expressed as

$$i(\vec{r}) = \frac{1}{2} \sum_{ij} \int dE \cdot G_{ij}^<(E) \lim_{\vec{r} \rightarrow \vec{r}'} (\nabla' - \nabla) \phi_i(\vec{r}') \phi_j^*(\vec{r}) \quad (2.3)$$

here r is the distance from the bond axis, ϕ_i s are atomic basis sets, and $G_{ij}^<(E)$ is the matrix correlation function. With the Hamiltonian and atomic basis sets extracted from the DFT calculations via the SIESTA program [21], we obtained the current density distribution of a mono-atomic carbon chain [11]. The distribution is found to be axially symmetric and well fitted by $i(r) = Ar^3 e^{-r/\alpha}$. For different values of total currents, $i(r)$ only scales with the amplitude A , while α remains unchanged. Within the numerical scheme described above, one can construct the total spatial distribution of the current, and the magnetic field can be obtained via the Biot-Savart law.

2.3 Performance

With these provisions, we are ready to analyze the transport and magnetic properties of various GSD structures. Figure 2.2 depicts the typical behavior of the current

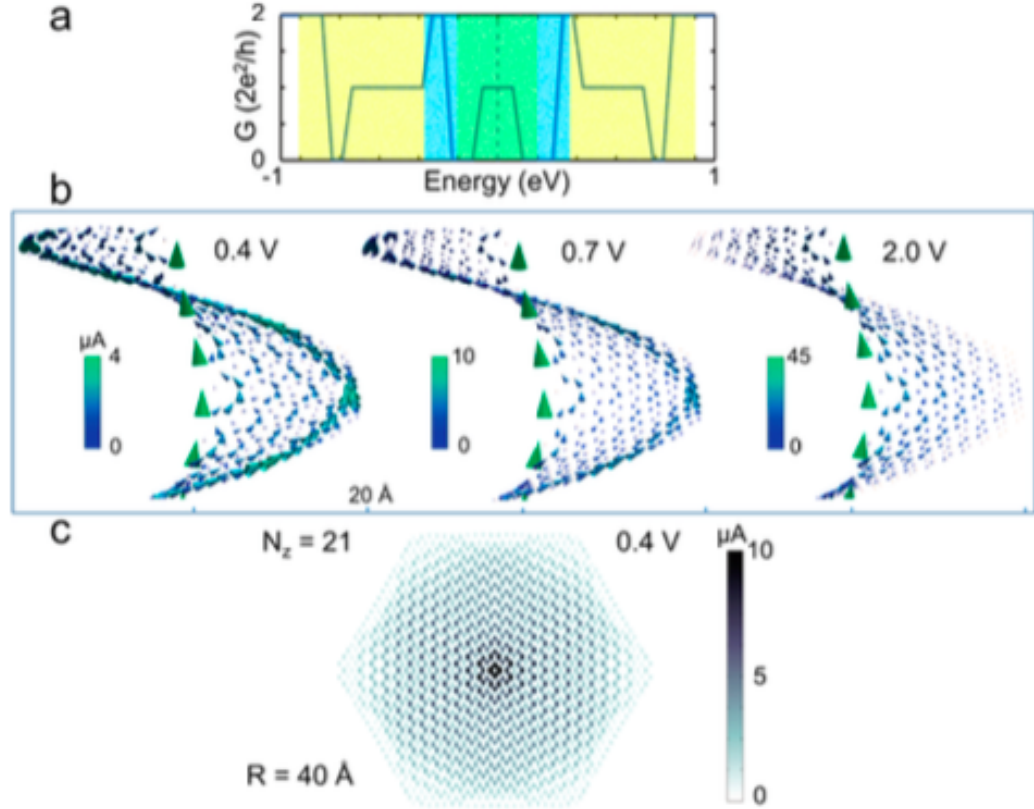


Figure 2.2 : (a,b) Metallic zigzag-edge ZGSD, $N_z = 9$. (a) Transmission coefficient as a function of energy. (b) Spatial current distribution integrated over various energy ranges of panel (a), left for green region (bias $V = 0.4$ V), middle for green plus blue region ($V = 0.7$ V), right for green plus blue plus yellow region ($V = 2$ V). (c) Bright-dark map of current distribution, for $N_z = 21$ and bias of 0.4 V. (Reprinted (adapted) with permission from F. Xu *et al.*, *Nano Letters*, 16,1,34-39, 2016. Copyright 2016 American Chemical Society.)

distribution in ZGSDs, with respect to width and applied voltage. As can be seen, in single-channel mode (green region in Figure 2.2(a)) the currents flow along the multi-

ple concentric circles, Figure 2.2(b) , left. Although the core hexagon plays a leading role in transport, the currents do not decrease monotonically toward the exterior but the perimeter zigzag edge carries substantial currents as well. Second, when the rising voltage opens the second double-channel (light-blue in Figure 2.2(a)), the current vectors almost disappear except those around the core and the ones at the outer zigzag edge, as shown in Figure 2.2(b), middle. The phenomenon of current-carrying edge is consistent with the decomposition of wave functions around the Fermi level; previous analytical study also demonstrated that in a semi-infinite graphene sheet the Bloch states around the Fermi level are localized at the zigzag edges [16]. The third stage, that is, the energy region up to the yellow in Figure 2.2(a) is engaged, the incremental currents mostly distribute around the core hexagon but attenuate toward the outer edge, as indicated in Figure 2.2(b), right; this remains the case thereafter for higher voltages. The outer-edge currents contribute significantly within the energy window of the first single-channel mode, which however shrinks for greater outer radius. If the radius is sufficiently large, the currents in the outer-edge bonds are negligible even when the bias is quite low, as shown in Figure 2.2(c). Accordingly, the zigzag-edge transport contributes only for a relatively small cross-section and under low bias. Such change of current distribution pattern with voltage constitutes a nonlinearity which must further lead to nonlinear inductance, as discussed below. Figure 2.3 further depicts the behavior of the magnetic field, magnetic flux and inductance of ZGSDs, also with respect to width and applied voltage. In Figure 2.3(a) shows calculated magnetic field for ZGSD of $N_Z = 9, 21$. The dashed blue line is obtained by simply scaling the curve of 0.5 V (solid blue) to fit its maximum with that of the red curve, as actually computed. Apparently, at smaller cross sections, the magnetic field fluctuates significantly, and at any point (except the axis) its value grows with the total

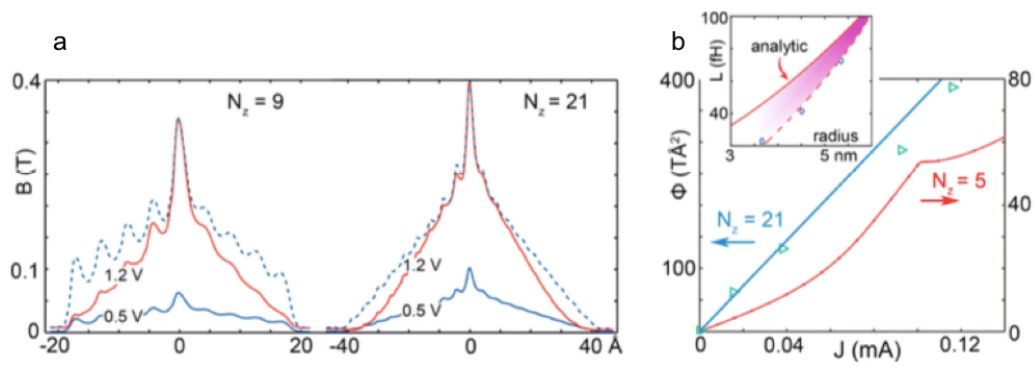


Figure 2.3 : (a)Magnetic field B versus the radial position. The dashed blue lines are obtained by simply scaling the curves of 0.5 V (solid blue) to highlight the deviations from the red curves, actually computed for 1.2 V. For a wider GSD ($N_z = 21$) the field rise is closer to proportional while change in the pattern lessens. (b)The magnetic flux Φ versus the total current J in a metallic ZGSD of small width $N_z = 5$ (red) and wider $N_z = 21$ (green triangles, fitted by the ohmic-solenoid formula, blue line). (Inset) Computed inductance for the atomistic models (circles) and the red curve from the classical model per eq 2.1. (Reprinted (adapted) with permission from F. Xu *et al.*, *Nano Letters*, 16,1,34-39, 2016. Copyright 2016 American Chemical Society.)

current not linearly, but more slowly. When the cross-section becomes sufficiently large, the fluctuations are smoothed out, and the $B(J)$ relation at each point is closer to linear. With the magnetic vectors available at any given point one can compute the magnetic flux $\Phi = \int B(r)2\pi r dr$ through a plane normal to the axis of a GSD, or energy $\mu_0^{-1} \int B^2(r)\pi r dr$ to determine the inductance L . We found that for some metallic ZGSDs with a small cross-section and minimum core $R' = 1.2\text{\AA}$, the flux is not simply proportional to the total current (Figure 2.3(b)), indicating that the inductance is a function of the total J , not a constant as for classical ohmic inductor. The turning points on the $\Phi(J)$ curves (shown example is for $N_Z = 5$) represent the change out of the first single-channel mode (cf. Figure 2.2(a)), when the contribution of the edge lowers while the currents start to concentrate around the core. A nonlinear inductance of metallic ZGSD has a distinct physical origin, as discussed above; the edge effect significantly alters the pattern of the current, whose value at a given lattice site is not simply linearly proportional to the voltage (and the total current), accordingly the distribution of the magnetic field across the solenoid varies and its resulting flux is not proportional to the current. When the ZGSD diameter is larger, the magnetic flux dependence on the total current gradually becomes linear, as shown for $N_Z = 21$ in Figure 2.3(a). The inset there shows that our computed flux remains lower than that of the analytical model (continuous ohmic), approaching it as the radius grows. Therefore, we can infer that when it comes to practical cases in which the cross-section can be regarded as infinite, the magnetic field at each point will vary linearly with the total current, and the inductance will be consistent with the prediction of eq 2.1. Finally, we give a quantitative estimate to show the superior solenoid performance of GSDs compared to typical existing inductor designs. For an integrated planar polygon spiral inductor with 8 turns, $3.0\text{ }\mu\text{m}$ turn spacing, 6.5

μm turn width, and $205\ \mu\text{m}$ outer diameter, the inductance is $7.3\ \text{nH}$, while a GSD with the minimum inner radius $1.2\ \text{\AA}$ and a normal thickness $1\ \mu\text{m}$ requires only an outer diameter of $70\ \text{nm}$ to produce the same inductance. Its parasitic capacitance, roughly estimated as for serially connected [3] numerous turn-to-turn plates capacitors, is only $3.4 \times 10^5\ \text{fF}$; the planar spiral inductor in the above example has a much greater $45\ \text{fF}$. Therefore, the parasitic capacitance of a GSD is negligible compared to spiral inductors, owing to the tiny cross-section and the massive number of turns. Note that according to eq 2.1, the larger inner radius will increase the inductance, while the parasitic capacitance will be lessened.

Chapter 3

Pseudo-Magnetic Field in Graphene

In this chapter, the phenomenon of strain-induced pseudo-magnetic field in graphene structures will be demonstrated. In 3.1,3.2 I will discuss the theory and also its macroscopic manifestation as Landau levels in the graphene electronic states. In 3.3 I will discuss two numerical schemes to model this effect in large graphene structures (with number of atoms $N \sim 10^5$).

3.1 Strain Induced Gauge Field in Graphene

A thorough review on the many strain-induced physical phenomena in graphene, and also its mathematical formalisms was already given by Sasaki et al [19]. Adapted from Sasaki's work, I will present a rather brief introduction and formalism to the strain induced pseudo-magnetic field(PMF) in graphene. Under a tight-binding framework, as shown in fig 3.1, with only nearest neighbor hopping considered, the Hamiltonian for graphene is expressed as

$$H_0 = -\gamma_0 \sum_{i \in A} \sum_{a=1,2,3} [(c_{i+a}^B)^\dagger c_i^A + (c_i^A)^\dagger c_{i+a}^B]$$

where $\gamma_0 \approx 2.7\text{eV}$ is the nearest neighbor hopping parameter, c_i^\dagger, c_i are the creation and annihilation operators at the i_{th} site, and A,B denote the A and B type of carbon atoms in a graphene lattice, separated by the lattice parameter a_{cc} . By Diagonalizing the Hamiltonian H_0 with the Bloch wavefunction one will find that the conduction band and valence band will meet at the K point, where $\mathbf{k} = \mathbf{k}_F = (4\pi/3a, 0)$ and

the K' point where $\mathbf{k} = -\mathbf{k}_F$, forming the well-known cone-like band structure. By Taylor expanding the Hamiltonian matrix element near the K and K' points, one can write an effective-mass Hamiltonian near K, K' points as

$$\begin{aligned} H_0^K &= v_F \boldsymbol{\sigma} \cdot \hat{\mathbf{p}} \\ H_0^{K'} &= v_F \boldsymbol{\sigma}' \cdot \hat{\mathbf{p}} \end{aligned} \quad (3.1)$$

which is strikingly similar to the Dirac equation for massless fermions or, the Weyl's equation. Here $v_F = 3a_{cc}\gamma_0/2\hbar \approx 10^6 \text{m/s}$ is called Fermi velocity. $\boldsymbol{\sigma} = (\sigma_x, \sigma_y)$ and $\boldsymbol{\sigma}' = (-\sigma_x, \sigma_y)$ consist of components of Pauli matrices, and $\hat{\mathbf{p}} = -i\hbar\nabla$ is the momentum operator.

By applying strain to graphene, one effectively imposes a perturbation to the hopping

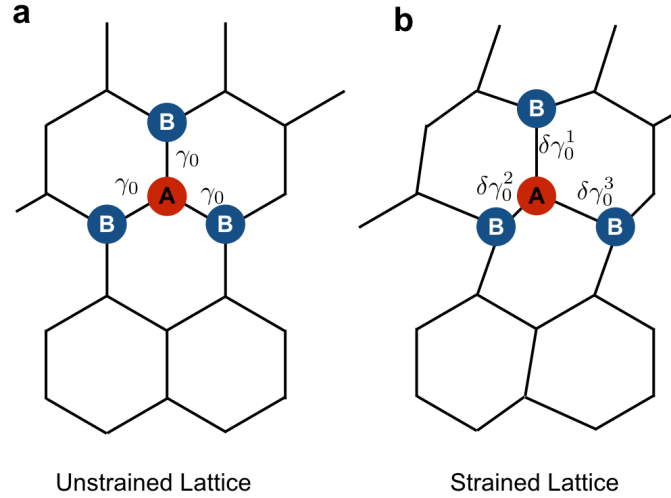


Figure 3.1 : Shows the schematics of (a)unstrained and (b)strained graphene lattice structure

parameters $\gamma_0 \rightarrow \gamma_0 + \delta\gamma_0$. The perturbation Hamiltonian can be expressed as

$$H_1 = \sum_{i \in A} \sum_{a=1,2,3} \delta\gamma_0^a(\mathbf{r}_i) [(c_{i+a}^B)^\dagger c_i^A + (c_i^A)^\dagger c_{i+a}^B]$$

The perturbation Hamiltonian causes scattering among the original Bloch wavefunctions, i.e. a state in the Brillouin zone \mathbf{k} will be scattered into $\mathbf{k}' = \mathbf{k} + \delta\mathbf{k}$. For

$\mathbf{k} = \mathbf{k}_F$ (or $-\mathbf{k}_F$), it can be shown that for large $\delta\mathbf{k}$, which means intervalley scattering between the K, K' points, does not contribute to the formation of the pseudo-magnetic field. As for small $\delta\mathbf{k}$, which means intravalley scattering within the K (or K') valley, does lead to the presence of an effective gauge field in the Hamiltonian. In this case we can express the matrix element of the perturbed Hamiltonian near the K, K' points as

$$\begin{aligned} H_0^K + H_1^K &= v_F \boldsymbol{\sigma} \cdot (\hat{\mathbf{p}} + \mathbf{A}(\mathbf{r})) \\ H_0^{K'} + H_1^{K'} &= v_F \boldsymbol{\sigma}' \cdot (\hat{\mathbf{p}} - \mathbf{A}(\mathbf{r})) \end{aligned} \quad (3.2)$$

where

$$\begin{aligned} v_F A_x(\mathbf{r}) &= \delta\gamma_0^1(\mathbf{r}) - \frac{1}{2}(\delta\gamma_0^2(\mathbf{r}) + \delta\gamma_0^3(\mathbf{r})) \\ v_F A_y(\mathbf{r}) &= \frac{\sqrt{3}}{2}(\delta\gamma_0^2(\mathbf{r}) - \delta\gamma_0^3(\mathbf{r})) \end{aligned} \quad (3.3)$$

Eq 3.2,3.3 clearly shows the connection from the perturbed hopping parameters $\delta\gamma_0$ to the effective gauge field $\mathbf{A}(\mathbf{r})$. In addition, the strain induced magnetic field is defined as $\mathbf{B}(\mathbf{r}) = \nabla \times \mathbf{A}(\mathbf{r})$

3.2 Pseudo-Landau Levels

The macroscopic manifestation of the strain induced magnetic field in graphene can be realized in the creation of the pseudo-Landau levels. It is known that the energy for free electrons, under a strong and uniform magnetic field, will be quantized into separate energy levels, or, Landau levels [8]. For a uniform magnetic field $\mathbf{B} = B\hat{z}$, we can have $A_x = -B y$. According to eq 3.3 we can choose $\delta\gamma_0^2 = \delta\gamma_0^3 = 0$ and $\delta\gamma_0^1 = -v_F B y$ as the strain pattern. This shows that a linearly distributed strain pattern can produce a uniform strain-induced magnetic field in graphene.

Finally, the Landau levels due to a uniform magnetic field for linearly dispersed particles as electrons in graphene near the Fermi level, can be obtained to as [4]

$$E_n = \pm v_F \sqrt{2e\hbar B n} \quad n=1,2,3... \quad (3.4)$$

Therefore, at these positions, we should expect a flat band in the bandstructure, and also a distinctive peak in the density of states (DOS).

3.3 Numerical Simulation

As shown above, the low level tight-binding Hamiltonian of graphene can be easily diagonalized via Bloch theorem. For a higher level tight-binding Hamiltonian (next nearest neighbor, multi-orbitals), numerical diagonalization is also trivially simple. However, while strain is applied to the lattice, translational symmetry is broken and the Hamiltonian matrix is not circulant anymore. Bloch theorem is no longer applicable and direct diagonalization of the full Hamiltonian, an operation scaling as $O(N^3)$, becomes necessary, which is computationally prohibitive for large systems. For an energy spectrum of resolution $\Delta E=0.01$ eV, the k -point resolution is $\Delta k = \Delta E/v_F$. With the graphene lattice constant $a_c=2.46\text{\AA}$, the system size is $N = (a_c \cdot \Delta k)^{-2} = 268^2 \approx 10^5$. For even higher resolution, diagonalization of such huge matrix size becomes impractical.

One way to overcome this problem is to utilize the fact that the Landau levels of interest are near the Fermi level, which means that with the help of spectrum slicing algorithms, one can solve for only the eigenvalues near the Fermi level with much less computational cost. In this work we use the linear algebra library SLEPc [5]. With the Jacobi-Davidson algorithm implemented, SLEPc is able to solve for the eigenvalues around a target position. As shown in fig 3.2(a), we model a 256×256

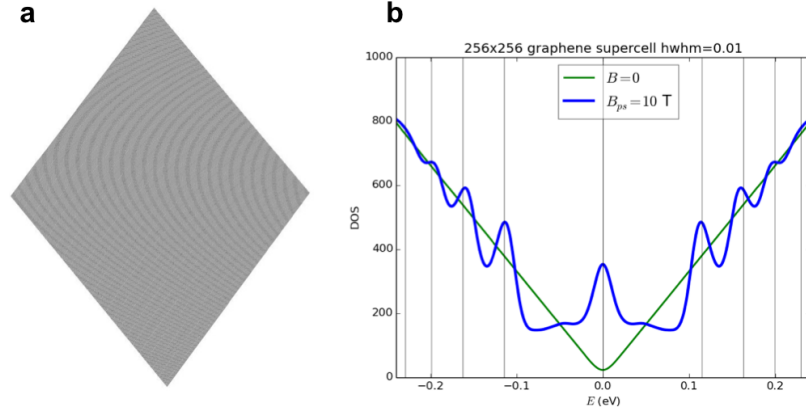


Figure 3.2 : (a) A 256×256 super cell of graphene flake. (b) DOS of unstrained (green) and strained (blue) graphene.

supercell of graphene, with the hopping parameters $\gamma_0(\mathbf{r})$ manually tuned to have a linear distribution, mimicking the effect of stretching the graphene flake, resulting in a strain-induced magnetic field $B = 10$ T. The calculated density of states (DOS) is plotted in fig 3.2(b). From the DOS plot one can clearly see that, while strained, certain peaks emerge around the Fermi level. To verify that these emerged peaks are indeed the Landau levels, we plot the energy levels predicted by eq 3.4 as vertical lines, which matches the peak positions in the DOS. These calculated results show that, as predicted in sections 3.1, 3.2, application of strain on graphene does induce an effective gauge field, and these effects are sufficiently captured via a single orbital, nearest neighbor Hamiltonian.

We now turn to a more realistic case but also very interesting way to overcome the computational challenge mentioned above. Apart from stretching, strain in graphene can also be induced by twisting the material. The advantage of studying a twisted graphene is two-fold. First, the strain profile of a twisted graphene ribbon, as shown in fig 3.3(a), can be calculated to be $\varepsilon = \sqrt{1 + (\alpha x)^2} - 1$, where α is the twisting

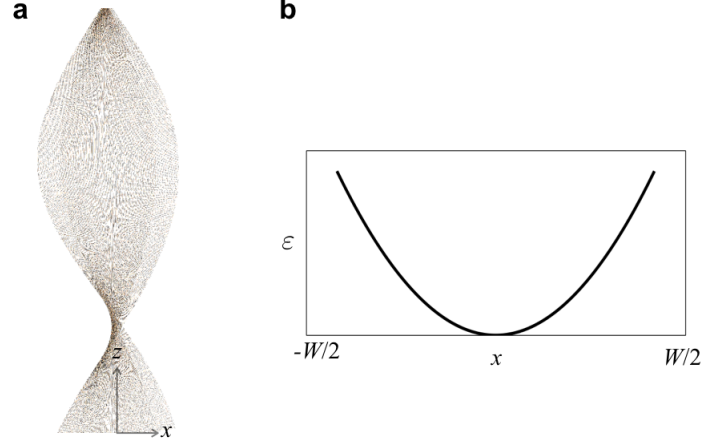


Figure 3.3 : (a) Atomistic structure of a twisted graphene ribbon. (b) Strain profile in a twisted ribbon.

rate and x is the in-plane distance perpendicular to the twisting axis z . As shown in fig 3.3(b), the strain profile is quadratic for small x ($\varepsilon \approx (\alpha^2/2)x^2$); as for large x , the strain becomes linear ($\varepsilon \approx \alpha^2 x^2$), which is desirable for the emergence of pseudo-Landau levels. Second, a very important feature of this system is its helical symmetry along the z axis. With a helical symmetry adapted Bloch theorem [25], the unit cell of a twisted ribbon can be reduced to a small size, allowing the study of huge systems. For instance, consider a zig-zag graphene ribbon with width $\sim 170\text{nm}$ (400 cells), with a twisting rate $0.61^\circ/\text{nm}$. The translationally symmetric unit cell for this system can be obtained by considering a full turn of the ribbon along z -direction, which is of length $\sim 590\text{ nm}$ in z , containing 3.8×10^6 carbon atoms in total. However, with the helical symmetry taken into account, the unit cell is reduced to only 0.24 nm of length in z , with a mere 1600 atoms in total, an astonishing reduction of system size for more than 1000 times. With these provisions we calculated the band structure and DOS of this twisted ribbon, which are shown in fig 3.4. In fig 3.4(a)(b) show the band structure and DOS of the untwisted graphene ribbon. In the band structure the

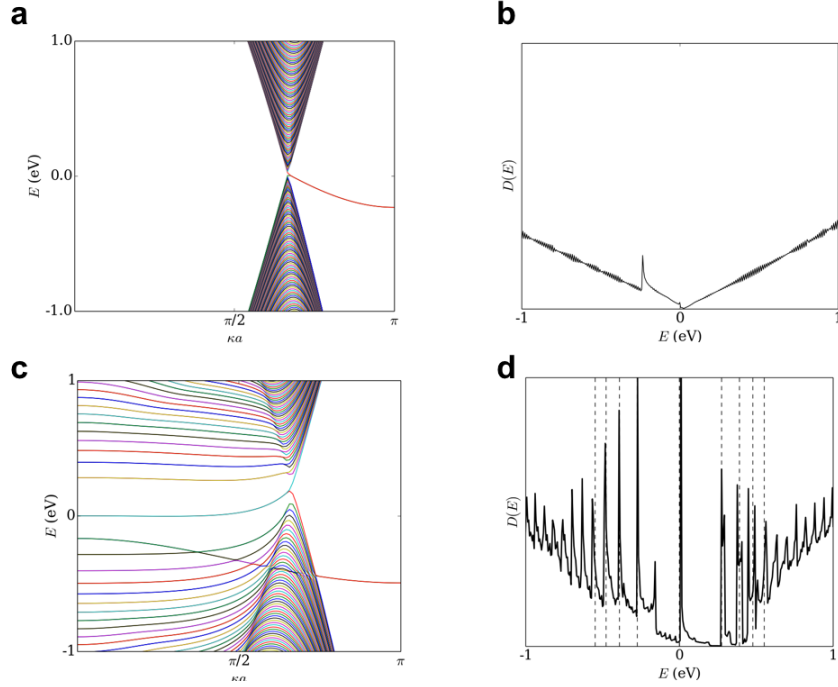


Figure 3.4 : (a) Band structure and (b) DOS of zig-zag graphene ribbon of width 170 nm. (c) Band structure and (d) DOS of twisted zig-zag graphene ribbon of width 170 nm and twisting rate $0.61^\circ/\text{nm}$. Dashed lines are plotted according to eq 3.4, with $B=60\text{T}$.

linear dispersion of graphene (Dirac cone) is clearly seen, with an additional out-lying band resulting from the zig-zag edge states. Similar features are also present in the DOS plot. The band structure of the twisted graphene is shown in 3.4(c), where one can still see clearly the original cone-like structure, with flat bands “pulled out” from the cone. These flat bands manifest themselves as sharp peaks in the DOS, which is plotted in fig 3.4(d). Here due to the applied strain, the original energy levels shown in fig 3.4(b) are quantized into the distinctive peaks shown in fig 3.4(d). The position of the quantized levels agree well with eq 3.4, with a strain-induced magnetic field of $B=60\text{T}$.

Chapter 4

2D Lateral Junction

In this chapter I will present a theoretical analysis of the electronic, electrostatic and doping behaviors of 2D lateral, coplanar junctions. The thermal equilibrium conditions of a heterojunction will be discussed in 4.1. In section 4.2 a brief introduction to traditional 3D junctions will be presented. In 4.3 the theory for 2D junctions will be shown, exemplifying the difference from its 3D counterpart. Finally, simulated results for real materials will be given in 4.4. Contents in sections 4.3 and 4.4 are mostly adapted from previously published work [28].

4.1 Thermodynamics of a Heterojunction

Regarding the thermodynamics of a heterojunction of two materials, the equilibrium conditions are the following [7]. The first condition is that the temperature is constant throughout the system, i.e. $T = \text{constant}$. A second condition can be obtained by maximizing the total entropy $S = S_1 + S_2$ with respect to the number of electrons in each system. Since the total number of electrons in the system $N = N_1 + N_2$ is constant, we can have

$$\frac{\partial S}{\partial N_1} = \frac{\partial S_1}{\partial N_1} + \frac{\partial S_2}{\partial N_1} = \frac{\partial S_1}{\partial N_1} - \frac{\partial S_2}{\partial N_2} = 0$$

by writing

$$dS = (1/T)dE - (\mu/T)dN$$

we can see that at equilibrium, for constant E and T we have $\partial S_i / \partial N_i = -\mu_i / T_i$ ($i=1,2$). Thus we have $\mu_1 / T_1 = \mu_2 / T_2$. Since in equilibrium $T_1 = T_2$, we have $\mu_1 = \mu_2$. The second condition for the equilibrium of a heterojunction is therefore

$$\mu = \text{constant} \quad (4.1)$$

The total chemical potential can be broken down into two parts $\mu = \mu^0 - \phi$ where μ^0 is the intrinsic chemical potential in the absence of external field, and ϕ is the electrostatic potential caused by the exchange of electrons between two materials. At equilibrium, we should expect regions within material 1 ($x \rightarrow -\infty$) to have $\mu^0 = \mu_1^0$, where μ_1^0 is the intrinsic chemical potential of material 1 before junction. Similarly we should expect in $\mu^0 = \mu_2^0$ in regions within material 2 ($x \rightarrow \infty$). This observation leads to

$$\Delta\phi = \phi(\infty) - \phi(-\infty) = \mu_2^0 - \mu_1^0 = \Delta\mu^0 \quad (4.2)$$

which shows that for the system to reach equilibrium, the exchange of electrons between two materials shall establish an electrostatic potential step throughout the heterojunction, balancing the difference between the intrinsic chemical potentials of two materials.

4.2 3-Dimensional Heterojunction

Now that we have established the criterion for thermal equilibrium of a heterojunction, we further relate these quantities with the charge density $\rho(x)$ by means of electrostatics. The electrostatics of 3D junction, being symmetric in 2 directions, is rather straightforward. From Poisson equation (in atomic unit) we have $\partial_x^2 \phi = -4\pi\rho(x)$, therefore we can write

$$\partial_x^2 \mu^0(x) = \partial_x^2 \phi(x) = -4\pi\rho(x) \quad (4.3)$$

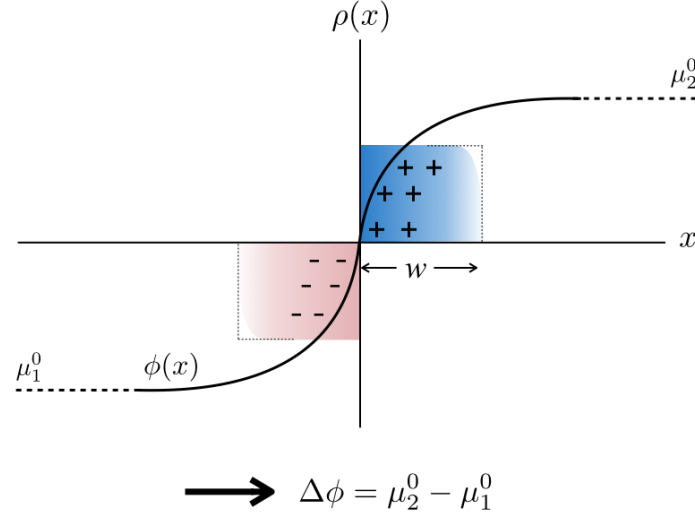


Figure 4.1 : 3D heterojunction of two materials with chemical potentials μ_1^0, μ_2^0 respectively. Charge exchange forms a dipole of width $2w$ at the interface, establishing an electrostatic potential $\phi(x)$ to equilibrate the system.

which shows that the charge density at point x is locally defined by the intrinsic chemical potential $\mu^0(x)$. This is a direct consequence of the strong screening in a 3D system. For a junction with a thin interface (such as metals), $\mu^0(x)$ is a step function, hence we have $\rho(x) = -(\Delta\phi/4\pi)\delta'(x)$, a charge dipole. This shows that the charge exchange in a 3D junction is in general highly localized. As for junctions of materials with moderate carrier density such as semiconductors, the interface will have a finite width w , which is called the depletion width. As shown in fig 4.1, within the depleted region, the charge density will reach the maximum value which is determined by the dopant level. There is also a transition region from the fully depleted zone to the neutral material, which is very narrow in 3D junctions. This justifies the common use of the abrupt depletion-layer approximation.

4.3 Theory of 2D Junction

In the description of a 2D lateral junction, while many of the properties regarding thermodynamic equilibrium can be successfully transferred from the 3D case, the electrostatics will be drastically different due to the dimensionality. As shown in

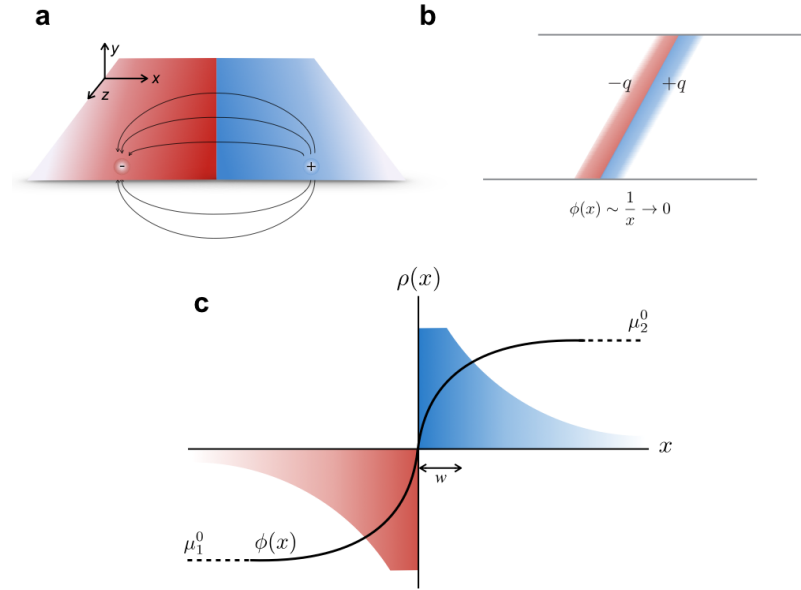


Figure 4.2 : (a) Schematics of a 2D lateral junction, showing how two in-plane charges can have long range interaction via out of plane direction. (b) Schematics of local charge exchange in a 2D junction forming a dipole line, which cannot establish a global potential step. (c) Shows that a delocalized charge exchange is required for the equilibration of the intrinsic chemical potentials.

fig 4.2(a), in-plane charges can interact via the out-of-plane direction, leading to long range interaction and extremely weak electronic screening in 2D systems. Moreover, if one assumes a localized charge transfer as in 3D case for a 2D junction, forming a dipole line as shown in fig 4.2(b), the potential will decay as $\sim 1/x$, not being able to establish a potential step necessary for equilibrium. This immediately means that a delocalized charge exchange is necessary for the establishment of the potential step

$\Delta\phi$ to balance the difference in the intrinsic chemical potentials $\Delta\mu^0$.

Many of the important distinctions between 3D and 2D junctions can be captured by the analysis of lateral heterojunction of two semi-infinite metal sheets. If the difference of their intrinsic chemical potential is $\Delta\mu^0 = \Delta\phi$, the 2D Poisson equation for the potential distribution $\phi(x, y)$ is:

$$\nabla^2\phi(x, y) = -4\pi\sigma(x)\delta(y) \quad (4.4)$$

with the boundary conditions $\phi(x = \pm\infty, y = 0) = \pm\Delta\phi/2$. Here x is the in-plane direction normal to the interface line z , y is the out of plane direction, and $\sigma(x)$ is the surface charge density, multiplied by $\delta(y)$ for a thin junction layer. Translational symmetry is assumed along z . We find that eq 4.4 is analytically solvable, with an elegantly simple solution $\phi(x, y) = \Delta\phi/\pi \tan^{-1}(x/y)$. The in-plane surface charge density $\sigma(x)$ is therefore given by:

$$\sigma(x) = -\frac{1}{\pi} \frac{\partial\phi}{\partial y} \Big|_{y=0} = \frac{1}{2\pi^2} \frac{\Delta\phi}{x} \quad (4.5)$$

The charge density is proportional to the chemical potential difference $\Delta\mu^0 = \Delta\phi$, and its singularity at the origin would be truncated by the carrier concentration in a real metal. The extensive tail $\sigma \sim 1/x$ is however a common feature of all lateral 2D heterojunctions. The necessity of the long charge tail in 2D junctions and even its functional form can be understood by estimating the integral of the electric field, $E(x) = 2\pi\sigma(x)$ at the surface $y = 0$ and then of nearly constant value over an arch-path connecting two remote points $\pm x$. The path length is πx , so that $2\pi^2\sigma(x) \cdot x = \Delta\phi$, which yields precisely eq 2. Note the diverging integral $\int_w^\infty \sigma(x)dx$, indicating the extensive charge transfer in a 2D junction, limited in reality by the device size L at the upper limit.

We also note that eq 4.5 contains no length scale at all to characterize the width

of the junction, unless a finite carrier density is introduced. The latter becomes essential when turning to p-n junction with carrier density limited by the dopant (areal) concentration $c = p/a^2$, p being probability of a dopant per unit cell of area a^2 . Accordingly the maximum carrier charge density is limited by $\sigma(x) \leq ec$. Combined with eq 2, one finds the width of depletion region as

$$W_2 = \frac{1}{2} \frac{\Delta\phi}{\pi^2 c} \sim \Delta\phi/p \quad (4.6)$$

Note that its scaling with the built-in potential and the dopant concentration is qualitatively different from that in a 3D junction, where $W_3 \sim (\Delta\phi/p)^{1/2}$ [22]. Yet more striking difference is in the extensive transition region $\sigma(x) \sim 1/x$, generally negligible in 3D junctions. Now that significant new features of 2D junction are captured, in the next section we go on to explore how it will be affected by specific material details in case of p-n junction in real semiconductor (e.g. MoS₂) or semimetal (graphene, Gr) or possibly their heterojunction (Gr|MoS₂).

4.4 Simulation of Real Material 2D Junction

For materials with a moderate carrier density (semiconductor, semimetal), eq 1.1 is no longer sufficient to obtain the potential and charge density, requiring a more material-specific account. Using full atomistic description such as the DFT is impractical [23]: as the above eqs 2-3 suggest and is shown below, depletion regions span very long range in 2D junctions, from 10 to 10⁴ nm which is orders of magnitude greater than in 3D; the standard plane wave basis used for extended systems imposes periodicity in all directions, requiring a supercell of at least 10²~10⁸ nm³ size . Instead, we employed a more manageable semiclassical approach [1] by considering the following

expression for the charge distribution $\sigma(x)$:

$$\sigma(x) = \sigma_+ + ec - \int_{-\infty}^{\phi(x)} C_q d\phi' \quad (4.7)$$

Here, the local charge density $\sigma(x)$ is obtained by adding the constant positive background from the host material (σ_+), and dopant ion concentration ($c = p/a^2$). The important variable third term represents the electrons stored by the layer intrinsic (quantum) capacitance C_q charged up to the local voltage $\phi(x)$ ($\phi(x, y = 0)$). This quantum capacitance is directly related to the density of states available to the electrons, $D(\varepsilon)$ or DOS: [12, 18] $C_q = \partial\sigma/\partial\phi = \int D(\varepsilon)(-\partial f(\varepsilon - \phi)/\partial\varepsilon)d\varepsilon$, where $f(\varepsilon)$ is the Fermi function. This expression relies on a rigid band approximation (RBA) for the DOS, i.e. $D(\varepsilon)$ independent of the local external potential $\phi(x)$ and charge $\sigma(x)$. To obtain the potential and charge distributions, eqs 1 and 4 are solved self-consistently. [9] By choosing the appropriate harmonic basis for the 2D Poisson equation, we are able to consider an infinite box length in the y direction, which is essential to capture the long-ranged features in a 2D junction. Use of RBA for the DOS is justified, as is clear from Figures 1c-d, which show full band structures of MoS₂ and graphene charged to $p = -0.1$ (red), 0.0 (black) and $+0.1$ (blue). The band structures change very slightly with charging, showing almost rigid bands under doping of ± 0.1 . Actual typical dopant levels are much smaller, from 10^{-6} to 10^{-3} , where the RBA is valid *a fortiori*. With these provisions we are ready to analyze two representative p-n junctions in monolayer semiconductors (MoS₂, Figure 1b) and semimetals (graphene, Figure 1c). Both junctions are assumed abrupt and having no interface states. For the p-n junction of MoS₂, the DOS near the band edges derives from the doubly degenerate parabolic bands originating from the K and K' valleys, with respective hole and electron masses of $m_h = 0.58 m$ and $m_e = 0.48 m$ [6, 20], m being the nominal electron mass; an experimental band gap of 1.85 eV [10] was assumed. The p- and n-

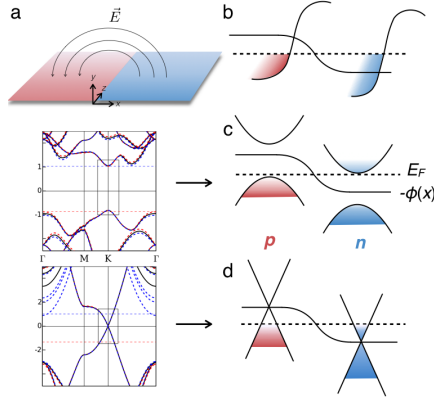


Figure 4.3 : Schematics of a lateral coplanar 2D heterojunction (a) and (b)-(d) of band alignments in the contacts of two metals (b), and semiconductor (c) or graphene (d) p-n junctions. E_F is the equilibrated Fermi level and $\phi(x)$ is the built-in potential within the plane of the materials. Full band structures of a 2D semiconductor (MoS_2) and graphene, with doping levels of -0.1 (red dashed), 0.0 (black solid) and +0.1 (blue dashed) e/cell are shown on the left. Horizontal lines show positions of the Fermi level for each doping degree. (Reprinted (adapted) with permission from H. Yu *et al.*, *Nano Letters*, 2016, doi:10.1021/acs.nanolett.6b01822. Copyright 2016 American Chemical Society.)

dopant ion concentration of $p = 10^{-4}$ was used symmetrically for MoS_2 , which results in a built-in potential of $\Delta\phi = 1.60$ V. To contrast the dimension-related behaviors more clearly, we also consider an equivalent hypothetical 3D semiconductor p-n junction with identical effective masses, band degeneracy, dopant concentration, and natural layer-spacing in y -direction. Other choices for the parameters of 3D materials are possible; however they do not alter the results significantly.

For the DOS of graphene near the Dirac point a linear dispersion $D(E) = (2/\pi\hbar^2v_F^2)|E|$ was used [2], with $v_F = 10^6$ m/s Fermi velocity. A dopant ion concentration $p = 1.5 \times 10^{-4}$ was applied symmetrically, resulting in a built-in potential of $\Delta\phi = 0.093$ V. The corresponding 3D p-n junction had graphene DOS and the natural interlayer spacing in y -direction is assumed. A temperature $T = 300$ K was used for the Fermi

function in all calculations. The Fermi level of all materials is assumed to be controlled by the dopant type and amount, given by the dopant concentration p . The

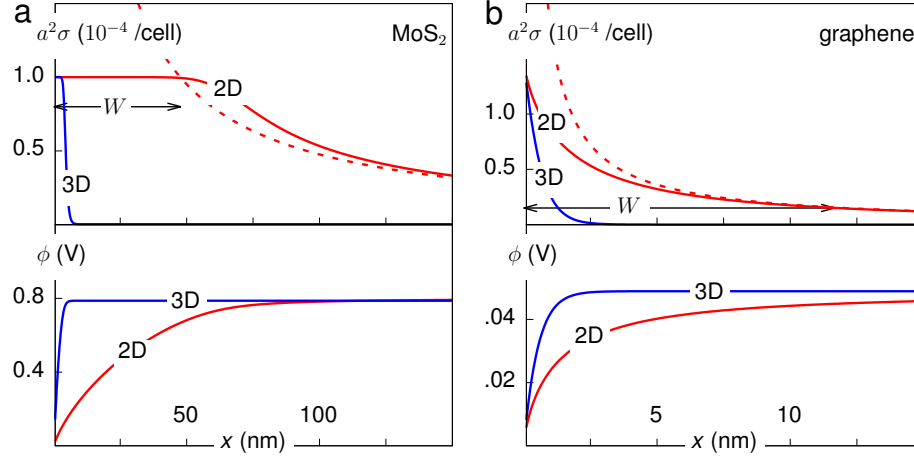


Figure 4.4 : Computed electrostatic potential and surface charge density in 2D lateral MoS₂|MoS₂ and graphene|graphene p-n junctions; only the n-doped side is shown. (a) Surface charge density (top) and electrostatic potential (bottom) for symmetrically doped 2D (solid red lines) and 3D bulk (solid blue lines) MoS₂ p-n junctions with doping $p = 10^{-4}$. The asymptotic behavior of eq 2 is shown with a red dashed line; the depletion width $W=48$ nm is marked. (b) Surface charge density (top) and electrostatic potential (bottom) for symmetrically doped lateral 2D and 3D bulk graphene p-n junctions with $p = 1.5 \cdot 10^{-4}$; width $W = 12$ nm of graphene junction is marked. (Reprinted (adapted) with permission from H. Yu *et al.*, *Nano Letters*, 2016, doi:10.1021/acs.nanolett.6b01822. Copyright 2016 American Chemical Society.)

calculated charge densities and electrostatic potentials are shown in Figure 3.2. Red solid curves plot solutions for 2D materials (MoS₂, graphene), red dashed curves are the asymptotic forms given by eq 2, and blue solid curves correspond to the 3D junctions. The charge distribution in a coplanar MoS₂|MoS₂ p-n junction is shown in the top panel of Figure 2a with a solid red line. The fully depleted area with constant charge near the contact transitions into a long charge tail extending into the material, approaching the asymptote $\sim 1/x$ (dashed red line) as predicted by eq 2. The deple-

tion width W , defined as a distance to the intersection of the full depletion level and perfect metal solution, is ~ 48 nm for this case. In contrast, the charge distribution in the corresponding 3D junction (solid blue line) drops rather abruptly at ~ 5 nm, without long tail. The potential profile in a $\text{MoS}_2|\text{MoS}_2$ p-n junction, shown in the bottom panel of Figure 2.2a with a solid red line, reaches the asymptotic value over the length of more than 60 nm. The potential varies rather slowly, change of $\Delta\phi/2 = 0.8$ V over 192 unit cells of MoS_2 amounts to 4 meV per unit cell. This contrasts with the potential in the bulk junction (solid blue line) reaching the asymptotic value at just ~ 4 nm. The fully depleted region is absent in gapless graphene, and the charge density in Figure 2b decreases gradually, approaching $\sim 1/x$ behavior at ~ 10 nm. We define the width of graphene junction as W where $\sigma(W) = 0.1 \cdot p/a^2$, which yields $W = 12$ nm. In contrast, the charge density for the corresponding 3D junction (solid blue line) drops rather quickly within 2 nm, without a long tail. The potential profile for $\text{Gr}|\text{Gr}$ p-n junction (solid red line in the bottom of Figure 3.2b) approaches the asymptotic value at ~ 10 nm. This corresponds to the $\Delta\phi$ gradient of 1.1 meV per unit cell, small enough to justify using ϕ as a parameter in the RBA for this system. It is clear from Figure 3.2 that in both examples of MoS_2 and Gr the depletion widths of 2D junctions are much greater than those of 3D analogs. More importantly, an extensive charge transfer with a $1/x$ charge tail is present in 2D junctions, while in 3D the charge transfer is localized and drops rapidly to zero over a small distance. These qualitative differences between the 2D and 3D junctions would be reflected in their response to the applied voltage. According to eq 3, the depletion widths scale as different powers of the built-in potential, $W \sim \Delta\phi^{1/d-1}$ with $d = 2$ or 3 , for the 2D or 3D cases. When the forward bias V is applied, the potential step becomes $\Delta\phi - V$, allowing one to determine how the depletion width W depends on the bias voltage,

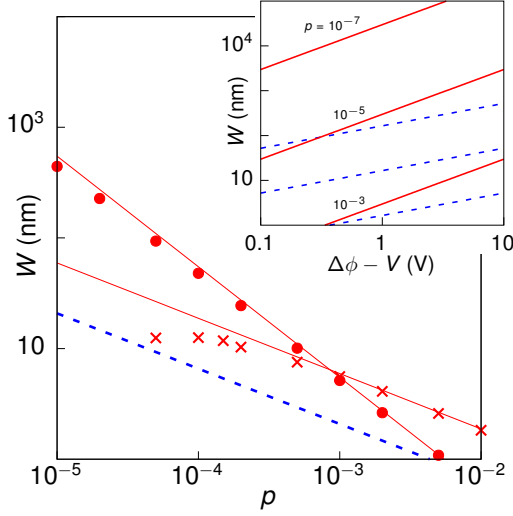


Figure 4.5 : The depletion width W in MoS₂| MoS₂ and Gr|Gr p-n junctions. Red circles show computed widths W_2 of lateral 2D MoS₂ junctions, and the red solid line is from eq 3; blue dashed line shows the depletion width W_3 of a corresponding 3D semiconductor. Red crosses, and the tracking red line show similar results for graphene. Inset compares the depletion widths of 2D (red lines) and 3D (blue dashed lines) semiconductors as functions of the total built-in potential $\Delta\phi - V$; depletion widths W_2 for 2D (red lines) and the widths W_3 for the 3D analog (blue dashed lines) are shown for $p = 10^{-7}, 10^{-5}$, and 10^{-3} . (Reprinted (adapted) with permission from H. Yu *et al.*, *Nano Letters*, 2016, doi:10.1021/acs.nanolett.6b01822. Copyright 2016 American Chemical Society.)

using eq 3. The depletion width can be measured indirectly through differential capacitance of the junction. For traditional 3D junctions the differential capacitance is given by $C_{3D} \sim p^{1/2}(\Delta\phi - V)^{-1/2} \sim W_3^{-1}$. [22] The capacitance of a 2D junction has a different form. For a 2D junction of finite total length L with the total charge Q (per transverse length) the capacitance $C_{2D} = dQ/dV$ can be calculated using eqs 2-3 as $C_{2D} = (1/2\pi^2) \ln(L/W_2)$. This yields an exponential relation, $W_2 = L \exp(2\pi^2 C_{2D})$, between the depletion width of a 2D junction and its measured capacitance. Figure 3 shows the computed W_2 for both junctions as a function of doping level p . The computed widths are plotted with red circles (for MoS₂) and red crosses (for Gr),

with the corresponding predictions of eq 3 shown as thin lines. For a semiconductor like MoS₂, the built-in potential $\Delta\phi$ is mainly determined by the band gap, with only small change due to doping, i.e. $\Delta\phi \approx \text{const}$ and, according to eq. 3, the depletion width changes as $\sim p^{-1}$, in close agreement with the computed data in Figure 3. In graphene, where DOS is decreasing near the Dirac point, the built-in potential depends strongly on the dopant concentration. The relation between the built-in potential and doping can be expressed as $p = \int_0^{\Delta\phi/2} D(E)dE = (1/\pi\hbar^2 v_F^2)\Delta\phi^2$ if temperature is ignored, which gives $\Delta\phi \sim p^{1/2}$. Substituting into eq 3, we have $W_2^{\text{graphene}} \sim \Delta\phi/p \sim p^{-1/2}$, which is also in close agreement with computed values in Figure 3 for high doping ($p > 10^{-4}$). For low doping, the built-in potential $\Delta\phi$ for graphene becomes comparable to the thermal energy $k_B T = 26$ meV. In this region the carriers are created predominantly by thermal excitations and the W reaches a plateau at $p < 10^{-4}$.

Chapter 5

Summary

In summary, I explored the interesting features and physics of 2D materials, and also their possible applications. Although many interesting problems have been solved, they also open ways to more exciting and challenging ones. For example, the multi-level numerical scheme employed in chapter 2 provides information of the current distribution, which is a powerful tool for the study of the electro-magnetic properties of large nano-structures. In chapter 3 the Landau quantization of the Dirac fermions in graphene caused by strain was shown and realized numerically. In the future, the possibility of large scale modeling and prediction of realistic devices will be explored. Finally, in chapter 4 I presented several universal features and scaling laws for 2D lateral junctions. In the future, I plan to explore the role of material specifics on top of these features. For example, how do interface states of different heterostructures affect the equilibrium state? Can we further describe the interface states in light of the topological band theory? Due to the abundant combinations of different materials, the room for further studies and investigations seem boundless.

Bibliography

- [1] N. Ashcroft and N. Mermin. *Solid State Physics*. Saunders College Publishing, 1976.
- [2] A. H. Castro Neto, F. Guinea, N. M. R. Peres, K. S. Novoselov, and A. K. Geim. The electronic properties of graphene. *Rev. Mod. Phys.*, 81:109–162, Jan 2009.
- [3] G. Grandi, M. K. Kazimierczuk, A. Massarini, and U. Reggiani. Stray capacitances of single-layer solenoid air-core inductors. *IEEE Transactions on Industry Applications*, 35(5):1162–1168, Sep 1999.
- [4] F. D. M. Haldane. Model for a quantum hall effect without landau levels: Condensed-matter realization of the "parity anomaly". *Phys. Rev. Lett.*, 61:2015–2018, Oct 1988.
- [5] V. Hernandez, J. E. Roman, and V. Vidal. SLEPc: A scalable and flexible toolkit for the solution of eigenvalue problems. *ACM Trans. Math. Software*, 31(3):351–362, 2005.
- [6] A. Kutana, E. S. Penev, and B. I. Yakobson. Engineering electronic properties of layered transition-metal dichalcogenide compounds through alloying. *Nanoscale*, 6(11):5820–5825, 2014.
- [7] L. Landau and E. Lifshitz. *Course of Theoretical Physics*, volume 5. Robert Maxwell, M.C., 3 edition, 1976.

- [8] L. Landau and E. Lifshitz. *Course of Theoretical Physics*, volume 3. Robert Maxwell, M.C., 3 edition, 1976.
- [9] F. m. c. Léonard and J. Tersoff. Novel length scales in nanotube devices. *Phys. Rev. Lett.*, 83:5174–5177, Dec 1999.
- [10] H. Liu, K. A. Antwi, S. Chua, and D. Chi. Vapor-phase growth and characterization of mo 1- x w x s 2 (0 x 1) atomic layers on 2-inch sapphire substrates. *Nanoscale*, 6(1):624–629, 2014.
- [11] M. Liu, V. I. Artyukhov, H. Lee, F. Xu, and B. I. Yakobson. Carbyne from first principles: chain of c atoms, a nanorod or a nanorope. *Acs Nano*, 7(11):10075–10082, 2013.
- [12] S. Luryi. Quantum capacitance devices. *Applied Physics Letters*, 52(6):501–503, 1988.
- [13] K. Nakada, M. Fujita, G. Dresselhaus, and M. S. Dresselhaus. Edge state in graphene ribbons: Nanometer size effect and edge shape dependence. *Phys. Rev. B*, 54:17954–17961, Dec 1996.
- [14] K. S. Novoselov, D. Jiang, F. Schedin, T. J. Booth, V. V. Khotkevich, S. V. Morozov, and A. K. Geim. Two-dimensional atomic crystals. *Proceedings of the National Academy of Sciences of the United States of America*, 102(30):10451–10453, 2005.
- [15] T. R. S. A. of Science. Graphene – the perfect atomic lattice, October 2010.
- [16] E. S. Penev, A. Kutana, and B. I. Yakobson. Can two-dimensional boron superconduct? *Nano Letters*, 16(4):2522–2526, 2016. PMID: 27003635.

- [17] V. M. Pereira, A. H. Castro Neto, and N. M. R. Peres. Tight-binding approach to uniaxial strain in graphene. *Phys. Rev. B*, 80:045401, Jul 2009.
- [18] A. Rahman, J. Guo, S. Datta, and M. S. Lundstrom. Theory of ballistic nanotransistors. *Electron Devices, IEEE Transactions on*, 50(9):1853–1864, 2003.
- [19] K.-i. Sasaki and R. Saito. Pseudospin and deformation-induced gauge field in graphene. *Prog. Theor. Phys. Suppl.*, 176:253–278, 2008.
- [20] H. Shi, H. Pan, Y.-W. Zhang, and B. I. Yakobson. Quasiparticle band structures and optical properties of strained monolayer mos_2 and ws_2 . *Phys. Rev. B*, 87:155304, Apr 2013.
- [21] J. M. Soler, E. Artacho, J. D. Gale, A. García, J. Junquera, P. Ordejón, and D. Sánchez-Portal. The siesta method for ab initio order- n materials simulation. *Journal of Physics: Condensed Matter*, 14(11):2745, 2002.
- [22] S. M. Sze and K. K. Ng. *Physics of semiconductor devices*. Wiley-Interscience, Hoboken, NJ, 2007.
- [23] X. Tian, L. Liu, Y. Du, J. Gu, J.-b. Xu, and B. I. Yakobson. Variable electronic properties of lateral phosphorene–graphene heterostructures. *Physical Chemistry Chemical Physics*, 17(47):31685–31692, 2015.
- [24] T. N. Todorov. Tight-binding simulation of current-carrying nanostructures. *Journal of Physics: Condensed Matter*, 14(11):3049, 2002.
- [25] C. T. White, D. H. Robertson, and J. W. Mintmire. Helical and rotational symmetries of nanoscale graphitic tubules. *Phys. Rev. B*, 47:5485–5488, Mar 1993.

- [26] F. Xu, H. Yu, A. Sadrzadeh, and B. I. Yakobson. Riemann surfaces of carbon as graphene nanosolenoids. *Nano Letters*, 16(1):34–39, 2016. PMID: 26452145.
- [27] Y. Xue, S. Datta, and M. A. Ratner. First-principles based matrix green’s function approach to molecular electronic devices: general formalism. *Chemical Physics*, 281(2–3):151 – 170, 2002.
- [28] H. Yu, A. Kutana, and B. I. Yakobson. Carrier delocalization in two-dimensional coplanar p–n junctions of graphene and metal dichalcogenides. *Nano Letters*, 0(0):null, 0. PMID: 27414071.